

Tensile and Low-Cycle Fatigue Behavior of Laser Powder Bed Fused Inconel 718 at Room and High Temperature

Nadja Sonntag, Benjamin Piesker, Luis Alexander Ávila Calderón, Gunther Mohr, Birgit Rehmer, Leonardo Agudo Jácome, Kai Hilgenberg, Alexander Evans, and Birgit Skrotzki*

This study investigates the room- and high-temperature (650 °C) tensile and low-cycle-fatigue behavior of Inconel 718 produced by laser powder bed fusion (PBF-LB/M) with a four-step heat treatment and compares the results to the conventional wrought material. The microstructure after heat treatment is characterized on different length scales. Compared to the wrought variant, the elastic and yield properties are comparable at both test temperatures while tensile strength, ductility, and strain hardening capacity are lower. The fatigue life of the PBF-LB/M variant at room temperature is slightly lower than that of the wrought material, while at 650 °C, it is vice versa. The cyclic stress response for both material variants is characterized by cyclic softening, which is more pronounced at the higher test temperature. High strain amplitudes ($\geq 0.7\%$) at room temperature and especially a high testing temperature result in the formation of multiple secondary cracks at the transitions of regions comprising predominantly elongated grain morphology and columns of stacked grains with ripple patterns in the PBF-LB/M material. This observation and pronounced crack branching and deflection indicate that the cracks are controlled by sharp micromechanical gradients and local $\langle 001 \rangle$ crystallite clusters.

1. Introduction

Additive manufacturing of metallic materials (metal AM) is now a widely studied field in manufacturing technologies, subject of numerous research activities, and already finding industrial applications. Frequently cited benefits of metal AM include geometric design flexibility, mass customization, weight, and operating cost savings as well as opportunities for waste reduction, shortening of process chains, the possibility to produce parts with compositional gradients and integrated functionality, and for component repair.^[1–4] Laser powder bed fusion (PBF-LB/M) is the most widespread metal AM technology. PBF-LB/M also has the possibility to specifically adjust the microstructures (e.g., crystallographic textures, grain sizes, substructures) via the process parameters and even to generate appropriately graded microstructures (tailored to the operating conditions).


In terms of its application, manufacturing component for safety-critical applications is now also becoming a focus of interest.^[1,5] One major challenge, in particular, is ensuring the structural integrity and reliability of safety-relevant parts, such as for aviation, as a detailed understanding of process–structure–property correlations is still missing. Major challenges still exist in the evaluation of mechanical behavior, especially at high temperatures (e.g., creep, isothermal, or thermo-mechanical fatigue), and robust data on material properties is still lacking.^[3]

Metal AM is particularly attractive to produce expensive high-temperature metallic alloys used for a wide range of components in the automotive, energy, and aviation industry. The nickel–base superalloy Inconel 718 (short: IN718) investigated in this study is used, for example, in the high-temperature regions of gas turbines. Due to its excellent strength, creep, fatigue, and corrosion resistance between room temperature (RT) and 650 °C,^[6] it is the most extensively used Ni-based superalloy and is employed as cast or wrought material. Yet, IN718 is difficult to machine because of its high strength and toughness. The additive manufacturing of components made of IN718 thus promises a considerable cost advantage due to the savings in material as well as processing and machining.^[6]

N. Sonntag, B. Piesker, L. A. Ávila Calderón, B. Rehmer, L. Agudo Jácome, B. Skrotzki
Materials Engineering
Bundesanstalt für Materialforschung und –prüfung (BAM)
Unter den Eichen 87, Berlin 12205, Germany
E-mail: birgit.skrotzki@bam.de

G. Mohr, K. Hilgenberg
Component Safety
Bundesanstalt für Materialforschung und –prüfung (BAM)
Unter den Eichen 87, Berlin 12205, Germany

A. Evans
Non-Destructive Testing
Bundesanstalt für Materialforschung und –prüfung (BAM)
Unter den Eichen 87, Berlin 12205, Germany

 The ORCID identification number(s) for the author(s) of this article can be found under <https://doi.org/10.1002/adem.202302122>.

© 2024 The Authors. Advanced Engineering Materials published by Wiley-VCH GmbH. This is an open access article under the terms of the Creative Commons Attribution License, which permits use, distribution and reproduction in any medium, provided the original work is properly cited.

DOI: 10.1002/adem.202302122

The metal AM processes have now been optimized to such an extent that high-quality parts with low density of flaws (e.g., cracks, pores, inclusions) and low distortion can be produced, and grain morphology and size can be tailored. Mechanical characterization of metal AM alloys used to focus on basic loading scenarios (tensile strength, hardness) and then progressively moved toward fatigue and crack propagation. The focus has been more on high-cycle (HCF) rather than low-cycle (LCF) fatigue^[2] as well as the effect of typical AM defects (i.e., how pores affect fatigue strength in the stress-controlled, defect-sensitive regime). For LCF, however, microstructure plays a more important role in deformation and hardening capability. Since these aspects have often been studied only for RT,^[7–9] there is still a gap in understanding the behavior also at the more relevant high-temperature regime.

Classical high-temperature materials also require heat treatment to establish the optimum combination of strength, ductility, fatigue, and creep resistance via stabilization of grain boundaries, grain size, and precipitates (type, shape, size, density, distribution) at various scales. In fact, different heat treatment strategies have been developed and established for conventionally manufactured material variants. Applied to structures manufactured by means of an AM technology, the same heat treatment strategies may not lead to the desired result since heat treatments should be adjusted for the initial conditions of the microstructure, as it is practiced for example in the different heat treatments existing for cast and hot-formed components. Another example of tailored heat treatment is the high-temperature creep and dwell fatigue behavior, which require modified heat treatments because of the special dislocation substructures in AM materials.^[6] Therefore, the adaptation and optimization of possible heat treatments for AM materials are further and more current research topics.^[6,10–12] Comprehensive studies on the mechanical properties, in particular the LCF behavior at high temperatures on heat-treated AM variants, are still lacking.

This is also the case for IN718 manufactured by PBF-LB/M. A clear understanding of mechanical properties related to the PBF-LB/M-specific microstructure or damage is still missing. In addition, heat treatments are needed to produce the typical strength-enhancing phases without unnecessarily destroying the unique PBF-LB/M microstructures.

Due to the high cooling rates in the PBF-LB/M process, the primary strengthening phases γ'' and γ' cannot form.^[6] In addition, a dislocation cellular substructure forms and Nb, Ti, and Mo tend to segregate on the cell walls, so that Laves phases may form there. The δ phase ($\text{Ni}_3(\text{Nb,Ti})$) can precipitate along the cell and grain boundaries.^[6] The presence of δ phase, Laves phase, and grain boundary carbides may have adverse effects on mechanical properties.^[6]

Typical heat treatment strategies for different forming processes or with respect to special properties (resistance to creep, fatigue, etc.) were summarized in several publications.^[6,10,11] Some studies indicated that the δ phase on the grain boundaries may increase the creep resistance via grain boundary serration.^[13,14] Desvallées et al. investigated the influence of δ phase (amount, shape) on mechanical resistance.^[15] They found that the δ phase has a detrimental effect on creep rupture life while no direct effect on LCF life was evident. Li et al. studied the effect of δ phase on crack propagation under creep and fatigue.^[16] They

reported that the spherical δ phase at grain boundaries has a retarding effect on the initiation and propagation of grain boundary cracks during creep and creep–fatigue interactions at elevated temperatures. However, it should be noted that there is still a lot of discussion in the literature about the role of δ phase on creep and fatigue behavior at high temperature.

The present study aims to fill existing research gaps and develop a better understanding of the relationship between microstructure, fatigue loading, and damage behavior. The alloy IN718 studied here was manufactured using the PBF-LB/M process. Subsequently, a four-step heat treatment was performed, and the resulting microstructure is analyzed as part of the study. Tensile test characteristics at RT and 650 °C are determined and compared with a wrought IN718 alloy studied as a reference (REF). In addition, a comparison is made with literature results (also with the as-built condition from identical PBF-LB/M process, see Schröder et al.^[11]). The LCF behavior is characterized at the same temperatures for PBF-LB/M and the wrought material; particularly for the PBF-LB/M variant, the microstructural features relevant to LCF damage are investigated.

2. Experimental Section

2.1. Materials and Sample Preparation

Two variants of the Ni-based alloy Inconel 718 were used for comparative investigations of the mechanical behavior. One was an additively manufactured material produced by PBF-LB/M and the other was a conventionally manufactured wrought material used as reference (REF material).

2.1.1. PBF-LB/M Material

For the PBF-LB/M material, commercial gas-atomized IN718 powder (SLM Solutions Group AG, Lübeck, Germany) with a particle size distribution from 10 to 45 μm and mean diameter of 39.5 μm was used ($d_{10} = 25.50 \mu\text{m}$, $d_{50} = 37.60 \mu\text{m}$, $d_{90} = 57.07 \mu\text{m}$). Its nominal chemical composition according to the manufacturer certificate is given in **Table 1**. Rectangular prisms (13 mm \times 13 mm \times 112.5 mm) as shown in **Figure 1a** were built in vertical direction on a preheated baseplate ($T_{\text{sub}} = 200 \text{ }^\circ\text{C}$, AISI314) in argon atmosphere ($<0.1\% \text{ O}_2$) using an SLM 280 HL machine (SLM Solutions Group AG, Lübeck, Germany). The same bidirectional scanning strategy with 90° rotation between layers as in the study of Schröder et al.^[11] was used, in which the as-built condition was also extensively characterized. The processing parameters were chosen following the recommendations of the machine manufacturer: laser power $P = 350 \text{ W}$, scanning velocity $v = 800 \text{ mm s}^{-1}$, defocused spot size diameter $d = 140 \mu\text{m}$, layer thickness $\Delta z = 60 \mu\text{m}$, and hatch distance $h = 150 \mu\text{m}$.^[11] The interlayer time t_{ILT} was

Table 1. Nominal composition of IN718 powder according to the manufacturer certificate.

Element	Ni	Cr	Fe	Nb	Mo	Ti	Al	Co	Mn	Si	C
Mass%	54.00	17.96	18.04	5.19	3.10	0.94	0.47	0.08	0.09	0.08	0.05

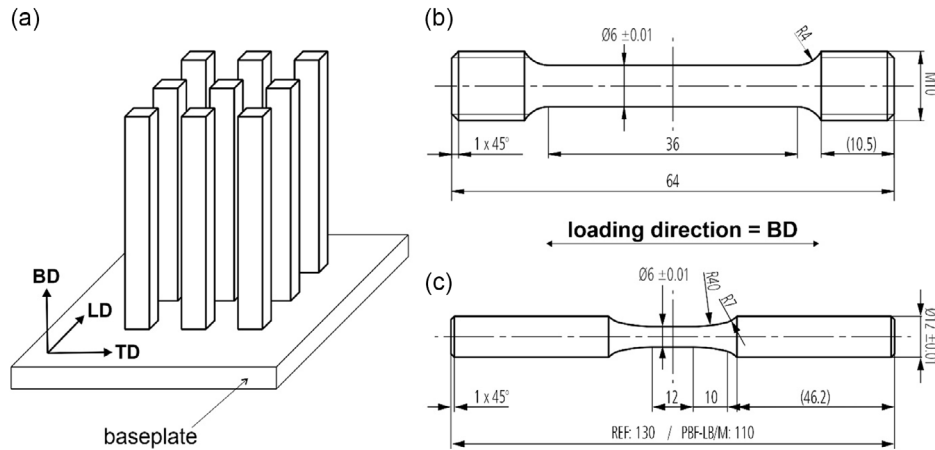


Figure 1. a) Coordinate system of the PBF-LB/M process (schematic). Sampling direction, geometry, and dimensions of b) tensile and c) LCF test pieces.

81 s.^[17] The actual composition of the PBF-LB/M material is given in **Table 2**. A small amount of gas porosity (<0.005%) was determined within the builds, as measured by X-ray computed tomography.^[11]

In contrast to Schröder et al.^[11] the PBF-LB/M material of our study was heat treated prior to specimen machining and mechanical testing. Here, the following substeps, combining standard heat treatments from ASTM F3301-18a^[18] for additive and AMS 5663:2022^[19] for wrought material variants, were applied to the blanks still on the baseplate under vacuum: 1) Stress relief/homogenization at 1065 °C was done for 1.5 h followed by air cooling to 50 °C to relax residual stresses, minimize distortion during specimen fabrication, and to reduce chemical microsegregations that may promote excessive δ phase formation during subsequent heat treatment steps. This step also reduces, particularly in terms of dislocation density, the cellular substructure inherent to the as-built condition; 2) Solutionizing at 965 °C for 1 h followed by forced air cooling to 50 °C to fully dissolve γ' and γ'' phases, which may have formed during previous step, while allowing limited intergranular δ precipitation for a presumed grain boundary strengthening; 3) Aging stage 1 at 720 °C for 8 h (followed by controlled cooling to aging stage 2 temperature) for γ'' precipitation was followed; and 4) Aging stage 2 at 620 °C for 8 h (followed by air cooling) for γ' precipitation.

The individual vertical prisms were cut from the baseplate by bandsaw after heat treatment.

2.1.2. Reference Material

The wrought reference IN718 material was manufactured by Enpar (Enpar Sonderwerkstoffe GmbH, Gummersbach,

Table 2. Actual chemical composition of PBF-LB/M IN718 analyzed by OES. Note: difference to 100% due to small amounts of other elements.

Element	Ni	Cr	Fe	Nb	Mo	Ti	Al	Co	Mn	Si	Cu
Mass-%	54.30	17.82	18.36	4.38	3.46	0.92	0.48	0.07	0.09	0.05	0.03

Germany) according to ASTM-B637:2018^[20] requirements and delivered as hot-rolled bar sections with a length of about 3.5 m and a diameter of 16 mm after conducting the following standard heat treatment (developed for high tensile and fatigue strength), according to AMS 5663:2022.^[19] 1) Solutionizing at 965 °C for 1 h followed by air cooling to 20 °C; 2) Aging stage 1 at 718 °C for 8 h followed by controlled cooling to aging stage 2; and 3) Aging stage 2 at 621 °C for 8 h followed by air cooling.

Its chemical composition according to the manufacturer certificate and according to own optical emission spectrometry (OES) analysis is summarized in **Table 3**. Minor deviations between certificate and OES results may be due to typical measurement uncertainties of OES of up to 10% and are not considered critical.

2.1.3. Test Pieces Used for Mechanical Testing

The rectangular prism on the base plate and the coordinate system of the PBF-LB/M process used in the following is schematically shown in Figure 1a. For simplicity, the abbreviations of the directions are used below, that is, build direction, BD, longitudinal direction, LD, and transverse direction, TD. Cylindrical tensile (Figure 1b) and LCF specimens (Figure 1c) were machined from the PBF-LB/M and REF materials, respectively. The rotational axes of the specimens were parallel to longitudinal rod axes of the REF material and parallel to the BD and centered with respect to the quadratic cross sections of the PBF-LB/M blanks. The lateral surfaces of the LCF specimens of both materials were longitudinally polished in the gauge length area with diamond

Table 3. Chemical composition in mass-% of conventional IN718 (REF) according to supplier certificate and own analysis by OES. Note: difference to 100% due to small amounts of other elements.

Element	Ni	Cr	Fe	Nb	Mo	Ti	Al	Co	Mn	Si	Cu
Certificate	53.70	17.82	18.26	5.21	3.02	0.93	0.53	0.16	0.14	0.08	0.04
OES	55.00	16.61	18.80	4.20	3.24	0.87	0.52	0.35	0.09	0.09	0.07

paste (6 μm grain size) to reduce the surface roughness prior to fatigue testing.

2.2. Mechanical Testing

2.2.1. Tensile Tests

The tensile tests were performed to characterize the general hardening and deformation capacity of the materials at room and elevated temperature. Two tensile tests per material variant and temperature were performed at RT and 650 °C on an electromechanical testing machine (Instron GmbH, Darmstadt, Germany; type 4505; class 1 calibration,) equipped with 100 kN force transducers. The RT tests were carried out according to DIN EN ISO 6892-1:2019^[21] method A using an axial extensometer (MTS systems; type 632.12C-21; class 1 calibration) of 25 mm nominal gauge length. Up to 10% engineering strain, the specimens were loaded at a constant strain rate of 0.00025 s⁻¹, and from 10% to fracture, at a constant crosshead speed of 0.009 mm s⁻¹. The high-temperature tensile tests were performed according to DIN EN ISO 6892-2:2018.^[22] Strain was measured by an axial water-cooled high-temperature extensometer (MTS systems; type 632.51C-05; class 0.5 calibration) with a nominal gauge length of 21 mm. These tests were conducted at a constant crosshead speed of 0.00252 mm s⁻¹ after preheating and specimen soaking was done at 650 °C for \approx 2.5 h in a three-zone furnace (Applied Test Systems, ATS). For temperature monitoring and control, two calibrated thermocouples (type S) were welded to the lower and upper radii of the specimens.

2.2.2. Low-Cycle Fatigue Tests

Symmetrical LCF tests were conducted under total strain control at a strain ratio of $R = -1$ and with a triangular waveform at RT and 650 °C on both material variants, following the recommendations in ISO 12 106:2017.^[23] A servohydraulic testing machine (MTS type 319.25 A T⁻¹, MTS Landmark, Eden Prairie, USA) equipped with calibrated 50 kN force transducers (class 1 calibration) and water-cooled, hydraulic collet grips was used for mechanical loading. Three strain amplitudes, ϵ_a (0.5%, 0.7%, and 0.9%) per temperature and material, were realized (one test per strain amplitude). Strains were measured and controlled by a water-cooled high-temperature extensometer with a nominal gauge length of 12 mm (MTS- 632.51F.04; class 0.2 calibration according to DIN EN ISO 9513:2012,^[24] MTS, Eden Prairie, USA). Specimen heating was carried out inductively using a high-frequency induction generator (TRUMPF SE + Co. KG, Ditzingen, Germany) that actuated a water-cooled copper coil. Due to the notch sensitivity of IN718, two calibrated thermocouples (type S) were welded to the lower and upper radii of the specimens (and not in the gauge length) for temperature monitoring and control, after the temperature profile along the specimen gauge length was determined in pretests on a reference specimen equipped with five thermocouples. After fatigue testing, the number of cycles to failure, N_f , was determined for each test by applying a failure criterion of 10% load drop of the maximum peak stress in the cyclic stress response curve versus number of cycles.^[23]

2.3. Microstructural Characterization of Heat-Treated Undeformed Material Conditions

2.3.1. SEM and EBSD

To identify characteristic microstructural features of the heat-treated PBF-LB/M material and enable comparisons with the nonheat-treated “as-built” condition (elucidated by Schröder et al.^[11]) as well as with the hot-rolled REF material, samples were extracted from the upper specimen heads of one LCF specimen each (for REF and PBF-LB/M), which was tested at RT. After sampling in the Cartesian coordinate system of the manufacturing process (cf. Figure 1a) using a low-speed laboratory wet cutting machine, three metallographic sections (LD–TD, BD–LD, BD–TD) for PBF-LB/M and two sections (longitudinal and cross section) for REF, respectively, were embedded in conductive epoxy resin (Technotherm 3000, Kulzer GmbH, Hanau, Germany) and metallographically prepared. Semiautomatic metallographic preparation comprised grinding at 320, 600, and 1800 SiC grit, polishing steps with 9, 3, and 1 μm diamond suspensions, and surface finishing using a 0.04 μm active oxide polishing suspension (OPS, Struers GmbH, Crinitz, Germany).

A scanning electron microscope (SEM, LEO Gemini 1530VP, Carl Zeiss Microscopy GmbH, Oberkochen, Germany), equipped with an electron backscatter diffraction (EBSD) Bruker Nano e-FlashHD detector (Bruker Corporation, Billerica, USA) and an energy-dispersive X-ray spectroscopy (EDS) detector (Bruker XFlash Detector 5030), was used for microstructural investigations at the microscale. To capture all relevant morphological and crystallographic features and the intrinsically heterogeneous nature of the additively manufactured PBF-LB/M material, EBSD scans and analyses were conducted at two different magnifications with a specimen tilt of 70° and using an acceleration voltage of 20 kV.

Characteristic microstructural features of both materials (see Figure 2 and 4) were visualized using Bruker ESPRIT 1.94 software package. However, since ESPRIT does not support any variation of the default misorientation (MO) angle of 5°, grain sizes were determined with the commercial software HKL Channel 5 (Oxford Instruments HKL, Hobro, Denmark). The corresponding EBSD parameters and threshold values used are summarized in Table 4. The minimum amount of pixel per grain was set to 217 pixels for the PBF-LB/M and to 10 pixels for REF material, considering the different grain sizes of the two materials. In addition, the parameters selected for the PBF-LB/M material facilitate comparison with earlier publications on a different material.^[25,26] For the conventionally manufactured REF material, the applied parameters were based on the recommendations of the ISO-Standard 13 067.^[27]

2.3.2. FIB, TEM, and STEM

To characterize the phases in the transmission electron microscope (TEM), an electron-transparent lamella was extracted from a suitable location in the region with predominantly elongated grain morphology, PEGM, (cf. Figure 2b) of the PBF-LB/M material via focused ion beam (FIB). The target location in the TD–LD plane (perpendicular to BD) was selected such that it

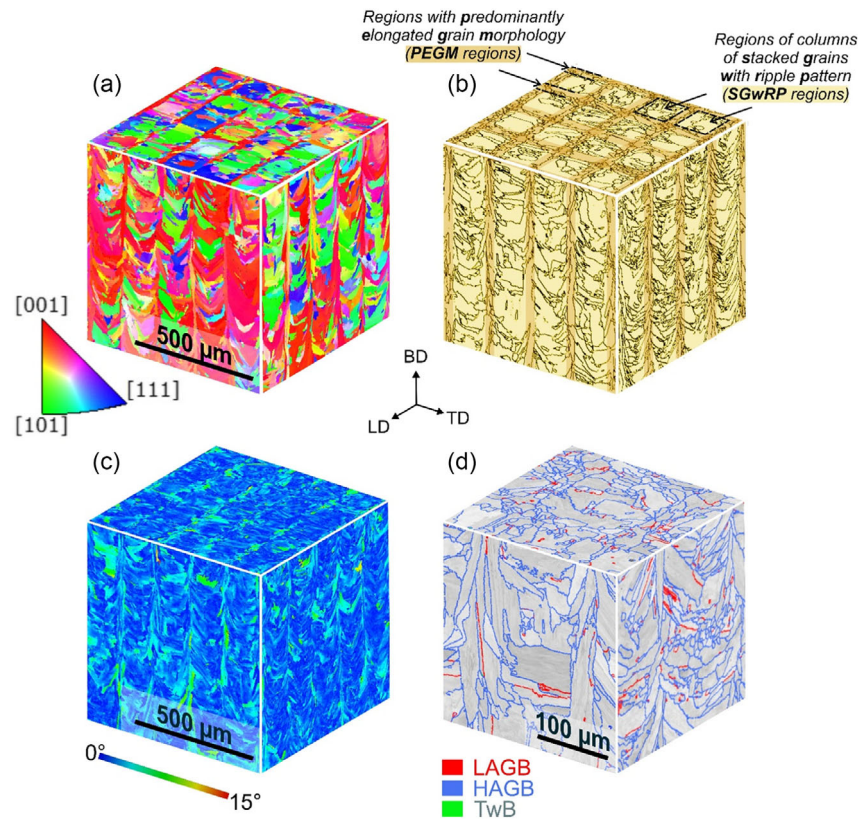


Figure 2. 3D representation of the microstructure of PBF-LB/IN718 after heat treatment. a) Orientation IPF maps, b) classification and designations used in the following for characteristic microstructural regions, c) MO average maps within grains, d) LAGB (red), HAGB (blue), and twin boundaries (TwB, green).

Table 4. Summary of EBSD parameters. MO = Misorientation. GB = Grain Boundaries. The map size is for all measurements 512×384 pixels.

	Section	Magnification	Pixel size [μm]	No. of analyzed grains	MO threshold [$^\circ$]	Grain size [μm]
IPF	LD–TD	250x	2.34	–	5	–
PBF-LB/M (Figure 2a)	BD–LD					
	BD–TD					
MO average PBF-LB/M (Figure 2c)	LD–TD	250x	2.34	–	5	–
	BD–LD					
Grain size PBF-LB/M	BD–LD	250x	2.34	160	10	60.9 ± 21.4
	BD–TD	250x	2.34	178	10	59.5 ± 21.7
	TD–LD	250x	2.34	166	10	59.2 ± 20.4
Grain size REF	BD–LD	1500x	0.39	535	10	6.87 ± 3.78
	TD–LD	1500x	0.39	583	10	6.51 ± 3.62
GB PBF-LB/M (Figure 2d)	LD–TD	750x	0.78	–	10	–
	BD–LD					
GB REF (Figure 4b)	LD–TD	1500x	0.39	–	10	–
	BD–LD					

had $\langle 001 \rangle$ orientations both into the depth of the metallographic sample (later height of the FIB lamella) and in the width of the lamella and that it also contained a high-angle grain

boundary (HAGB) with a δ phase (see marked area in Figure 3a). A Quanta 3D field-emission gun (FEG) FIB (FEI) was used for targeted preparation by applying a Ga source.

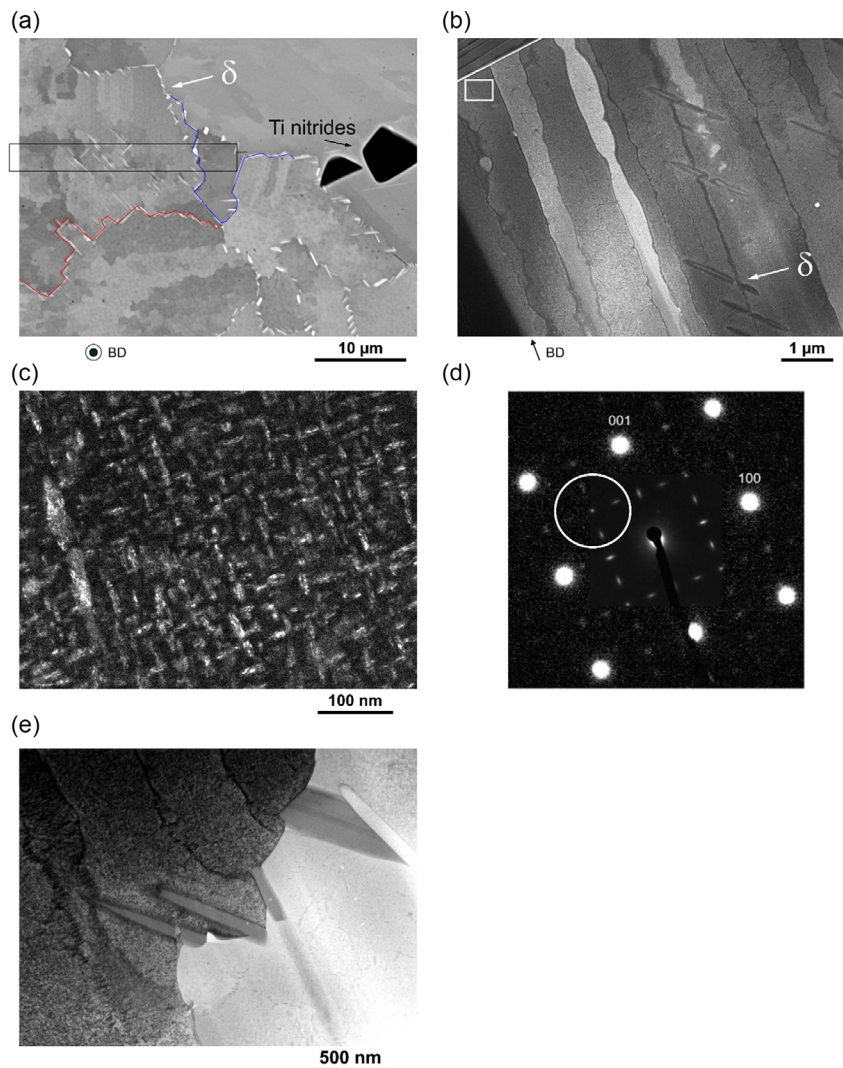


Figure 3. a) BSE–SEM image shows δ precipitates (bright) and nitrides (dark). Red and blue contours exemplify LAGB and HAGB, respectively. b) STEM–BF image of subgrains present in FIB lamella extracted from rectangular region marked in a). c) CTEM–DF image of γ'' precipitates of region marked in b), with corresponding selected-area diffraction pattern oriented along $[001]$ in d). e) STEM–BF of HAGB with δ needles.

Milling and thinning were performed at 30 kV and currents from 30 nA at the beginning down to 0.1 nA at the end. Finally, a double-sided finish was performed at 2 kV and 27 pA for 2.5 min.

TEM studies were performed at an accelerating voltage of 200 kV using a JEOL JEM 2200 FS microscope (JEOL Ltd., Japan) equipped with FEG, an “Omega”-type energy filter, and a scanning TEM (STEM) unit.

2.4. Follow-Up Investigations after Testing

2.4.1. Fracture Analysis

Fractured specimen halves of tensile and LCF specimens of both material states were imaged in a calibrated macrophoto stand to capture topographical features of the fracture surfaces and some special features on the lateral surfaces. In addition, fracture surfaces were examined in top view by optical microscopy (OM)

using a stereomicroscope with z-correction to better and more comparably image dimensions of different fracture areas.

Subsequently, the fracture surfaces of the LCF specimens were examined fractographically in the SEM (type Tescan Vega3) at an accelerating voltage of 20 kV using a backscatter electron detector BSE 4Q. Crack initiators, impurity phases, as well as grain orientations (by EBSD) were identified, and images were taken at higher magnification in fatigue crack areas with focus on damage at the transitions of regions with PEGM and of columns of stacked grains with ripple pattern (SGWRP, cf. Figure 2b).

2.4.2. Metallographic Analysis of Fatigue Crack Propagation

For these investigations, longitudinal sections were prepared by cutting the LCF specimens of the PBF-LB/M material along the

center parallel to the loading direction. The cutting machine used, the metallographic preparation, and the SEM applied have already been described in section 2.3.1. The specimens were examined nontilted in BSE mode at different magnifications to contrast orientation differences.

3. Results and Discussion

3.1. Microstructure of Undeformed Material States

3.1.1. PBF-LB/IN718

The microstructure of the PBF-LB/M variant is represented in Figure 2 and 3. The orientation (i.e., inverse pole figure (IPF) maps are shown in perspective as a cube in Figure 2a with normal vectors in BD, LD, and TD directions (the coordinate system is shown in the center of Figure 2).

The grain orientations are indicated by the color-coded crystallographic triangle at the bottom left of Figure 2a. The colors in the IPFs in Figure 2a indicate the crystal orientation that is parallel to the directions that in turn are perpendicular to each face of the schematic IPF cube, that is, to LD on left, TD on right, and BD on top faces. The investigated PBF-LB/IN718 features a heterogeneous but periodic grain structure with the two alternating characteristic microstructural regions, as classified in Figure 2b. This grain morphology can be directly related to the manufacturing process and is typical of the process parameters and scanning strategy used.^[2,28]

In face-centered cubic (fcc) metals, such as Ni-based alloys, grains tend to form during PBF-LB/M manufacturing by aligning with $\langle 001 \rangle$ direction during solidification parallel to the thermal gradient at the melt pool boundaries. This is attributed to the lower modulus of elasticity in $\langle 001 \rangle$ with respect to $\langle 110 \rangle$ and $\langle 111 \rangle$, which is linked to the atomic arrangement along these crystallographic directions.^[9,29] At the bottom of the melt pools and in combination with the used hatching strategy, this growing mechanism creates a narrow and elongated grain morphology (cf. PEGM regions in Figure 2b) parallel to BD (mostly with $\langle 001 \rangle \parallel$ BD; cf. thin red stripes in Figure 2a). The PEGM grains line up next to each other following the hatch pattern and produce the typical checkerboard pattern in the TD-LD plane (perpendicular to BD), with the hatch distance (here $h = 150 \mu\text{m}$) coinciding with the spacing between two

consecutive square centers. Where the melt pool boundary is less parallel to BD and the interlayer rotation during manufacturing reduces pronounced dendritic growth (and thus crystallographic anisotropy) in BD, columns of SGWRP regions, cf. Figure 2b, in the BD-LD and BD-TD planes form between PEGM regions and fill out the checkerboard squares perpendicular to BD.

Thus, the microstructure of PBF-LB/IN718 manufactured using a bidirectional scanning strategy is already heterogeneous within each examined plane in the Cartesian coordinate system of the manufacturing process and periodic to a certain degree. Depending on the sectioning plane, the microstructure differs because of the particular grain morphology (perpendicular to BD completely different from transverse to it), so that a slight macroscopic and, particularly, a micromechanical anisotropy must, though, be expected. Compared to the as-built state (cf.^[11]), both the typical alternating PEGM-SGWRP structure and the crystallographic texture remain unchanged, with the latter being weak and showing components $[011]/[001] \parallel$ BD and $[001]$ type along LD and TD.

The grain size was evaluated from EBSD measurements on sections parallel and perpendicular to BD. For grain size determination, near-edge grains were excluded. Further details of the grain size determination are listed in Table 4. The mean grain size identified by this procedure is around $60 \mu\text{m}$. The PBF-LB/M material is on average nearly one order of magnitude coarser grained than the REF material, for which a mean grain size of $\approx 6.7 \mu\text{m}$ was determined (cf. Figure 4). The grain sizes differ slightly from our previous data publication due to the smaller threshold used here (10° instead of 15°).^[30] However, the deviations remain within the common scatter.

Figure 2c shows the MO average map within grains for angles up to 15° . In this map, the average orientation of a grain is compared to the orientation of each pixel; the resulting difference, expressed in a MO value, gives the color for that pixel. This represents only a rough estimate, because, for an adequate EBSD MO analysis with accurate quantitative MO values, measurements would have to be made at higher magnification and smaller step size after accurate preparation. Since the standard angular resolution is limited and Kikuchi patterns are only stored in compressed form by standard software, additional reconstruction steps are often required for reliable MO analyses, see ref. [31], which were not performed in the context of this research. Nevertheless, the resolution is high enough to detect

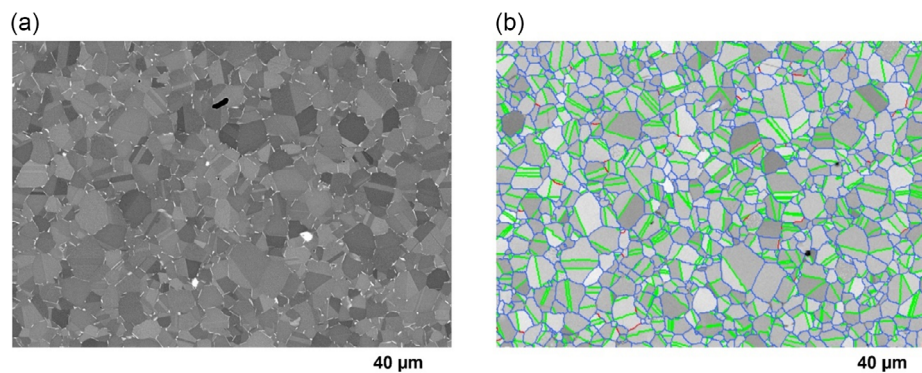


Figure 4. a) BSE image of microstructure (cross section) of REF material. b) Classified grain boundaries with same color code as in Figure 2d.

orientation gradients in sufficiently large grains. Therefore, the maps allow us to state that the PEGM regions (see checkerboard in TD–LD) and the regions around triple points (see side faces of the cube) are partly crystallographically disturbed even *before* mechanical loading (recognizable by the shades of green). Since the disturbed regions appear periodically in an otherwise less disturbed SGWRP region, and in some cases form correspondingly sharp gradients, it must be assumed that mechanical, chemical, and physical properties will be systematically site dependent in the PBF-LB/M material under study.

Figure 2d shows the grain boundaries classified by low angle grain boundaries (LAGBs, red), HAGBs (blue; twin boundaries excluded), and $\{111\}$ twin boundaries (TwB; green). To properly show the spatial distribution of the different grain boundary types, this analysis was performed with higher resolution and magnification than used for the previous microstructure cubes in Figure 2a,c (see Table 4). In contrast to typical as-built structures, HAGBs predominate (about 90% of all detected grain boundaries) in the heat-treated condition, and only a few LAGBs are visible. However, it should be noted that the limited resolution in EBSD must also be considered (LAGBs with MO angles $<2^\circ$ and subgrains in the nanometer range are not detectable by EBSD, if present). In contrast to the REF material, which has also been extensively characterized, there are virtually no twin boundaries here despite the heat treatment. Figure 2d also reveals the pronounced variation of the grain size: fine-grained clusters appear mainly in the regions of predominantly elongated grains intersecting TD–LD (along the checkerboard edges) and sporadically within the SGWRP regions perpendicular to BD (in the side faces of the cube). Recrystallization was not intended in the heat treatment, as the annealing temperature was chosen slightly below the recrystallization temperature. However, it cannot be safely ruled out that this may have happened locally since the as-built state had a high dislocation density. In any case, HAGBs defining tiny grains were corroborated.

The BSE–SEM image in Figure 3a visualizes the microprecipitates typical for IN718 such as acicular δ phase (orthorhombic, $\text{Ni}_3(\text{Nb,Ti})$) on the HAGBs (e.g., blue contour) and LAGBs (e.g., red contour) which are deliberately generated during heat treatment, as well as nitrides (black). The latter occasionally occur in the interior of the grains, but not in the frequency suggested by the image. In fact, the fine-grained region above the red and left of the blue contours was identified by complementary EBSD analyses (not shown here) as one of the thin regions with orientation $[001] \parallel \text{BD}$, which delineates the checkerboard squares (see Figure 2a). From this region, a TEM lamella was prepared by FIB perpendicular to the image plane along the location indicated by the black rectangle. Note that, while δ needles may also grow between subgrain structures that appear alternately in light and dark gray, where MOs are $<5^\circ$ (e.g., the TEM-lamella region), the subgrain boundaries are mostly free of δ phase. These δ needles between subgrain structures as well as the δ needles on the grain boundaries are rather small (length $\approx 1 \mu\text{m}$) in relation to the grain size. The typical microsegregation found in the interdendritic regions of the as-built condition (cf. Figure 4 in Schröder et al.^[11]) is significantly reduced after heat treatment.

The STEM bright-field (BF) image in Figure 3b within the extracted TEM lamella shows that the subgrains are elongated,

their boundaries are sharply defined, and are oriented along the BD. These subgrains resemble the original cellular structure that is characteristic of the as-built PBF-LB/IN718 state, with their width being $\approx 1 \mu\text{m}$. Some fine δ needles are also visible (white arrow) below the original metallographic surface. The conventional TEM dark-field (CTEM-DF) image in Figure 3c shows thin ellipsoidal disc-shaped precipitates (bright) of about 50 nm in length, which are identified as γ'' phase (bct, Ni_3Nb , coherent to γ matrix).

The corresponding selected-area diffraction pattern acquired along $[010]$ and given in Figure 3d confirms the precipitation of γ'' . Figure 3e (STEM-BF) shows a HAGB with some δ needles.

3.1.2. Wrought Reference Material

The grain structure of the undeformed reference material is shown in Figure 4. The grain morphology is equiaxed and more homogeneous than in the PBF-LB/M material and the grain size is much smaller ($\approx 6 \mu\text{m}$). The grain morphology is isotropic in LD and TD of the hot-rolled bar. δ phase needles (bright) are visible in Figure 4a at the grain boundaries, and a few Nb carbides are also present. The grain boundaries were characterized by the same procedure as for the PBF-LB/M material (cf. Table 4). It is clearly apparent in Figure 4b that the amount of LAGBs (red) is neglectable in the wrought material, and in contrast to the PBF-LB/M material, a high density of twin boundaries (green) is observed.

3.2. Mechanical Behavior

3.2.1. Tensile Tests

Representative results of the tensile tests at RT and at $T = 650^\circ\text{C}$ are shown in Figure 5 for both material variants. The slope of the elastic part of the stress–strain curve, m_E , is at both test temperatures slightly higher for the wrought than for the PBF-LB/M material (cf. Table 5). This is consistent with results of other studies, in which we performed more precise measurements of the temperature-dependent Young's modulus using the dynamic resonance method.^[17,30] Despite these slight differences in m_E , overall, the elastic behavior and the onset of yielding in terms of 0.2% proof strengths, $R_{p0.2}$, are comparable in the two variants. The characteristic values of all tensile tests performed are summarized in Table 5. At RT, the hardening capacity of the PBF-LB/M material is lower (Figure 5a) and is accompanied by correspondingly lower ultimate tensile strength and, above all, lower elongation at failure. At $T = 650^\circ\text{C}$, it is noticeable that practically no strain hardening is observed after yielding, as the stress decreases continuously for both variants (Figure 5b). At this temperature, the ductility of the PBF-LB/M variant is significantly lower than that of the REF condition. In addition, it exhibits greater softening.

Sabzi et al. showed in their investigations on PBF-LB/316L SS produced with different process parameters (i.e., heat input) that there is no clear correlation between yield strength and ultimate tensile strength with porosity content.^[32] They emphasized rather the significance of the influence of microstructure development and showed that yield strength and ultimate tensile

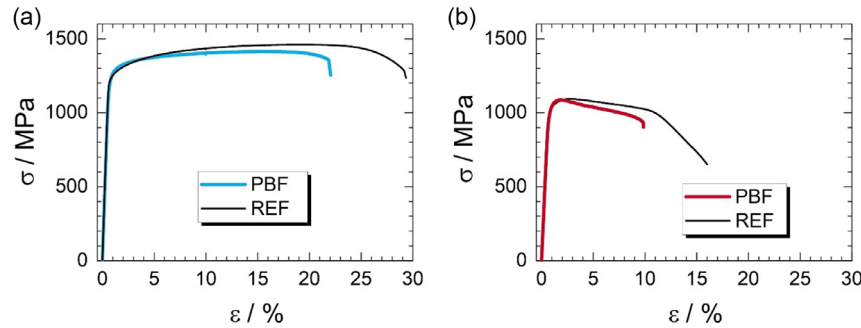


Figure 5. Engineering stress–strain curves at RT a) and at 650 °C b). PBF-LB/M material (blue, red) and wrought material (REF, black).

Table 5. Results of monotonic tensile tests at different test temperatures, T : slope of the elastic part of the stress–percentage extension curve, m_E , 0.2% proof strength, $R_{p0.2}$, tensile strength, R_m , elongation after fracture, A , reduction of area, Z .

Specimen ID	T [°C]	m_E [GPa]	$R_{p0.2}$ [MPa]	R_m [MPa]	A [%]	Z [%]	Manufacturing process/heat treatment
REF 18	20	212	1223	1460	28.5	41	Hot rolled, heat treatment as specified in section 2.1.2
REF 20	20	218	1221	1461	29.0	41	Hot rolled, heat treatment as specified in section 2.1.2
PBF-LB/M 11	20	203	1223	1413	21.0	28	PBF-LB/M, heat treatment as specified in section 2.1.1
PBF-LB/M 13	20	191	1221	1402	21.5	30	PBF-LB/M, heat treatment as specified in section 2.1.1
REF 23	650	174	1032	1143	^{a)}	31	Hot rolled, heat treatment as specified in section 2.1.2
REF 24	650	164	1007	1093	16.0	31	Hot rolled, heat treatment as specified in section 2.1.2
PBF-LB/M 17	650	155	1014	1087	9.0	14	PBF-LB/M, heat treatment as specified in section 2.1.1
PBF-LB/M 20	650	154	1001	1074	8.0	13	PBF-LB/M, heat treatment as specified in section 2.1.1
Schröder et al. ^[11]	RT	–	635	992	37	–	PBF-LB/M (same processing parameters as in this study, vertically built specimens), no heat treatment (as-built condition)
Piglione et al. ^[35]	RT	210	1253	1495	7.9	–	PBF-LB/M (same scanning strategy, different processing parameters, e.g., layer thickness of 30 μm , horizontally built specimens), comparable solution and precipitation annealing; no stress relief
Sharma et al. ^[12]	RT	213	1011	1268	26	–	PBF-LB/M (different processing parameters, e.g., layer thickness of 40 μm , different scanning strategy, vertically built specimens), double-stage solution heat treatment, two-stage precipitation hardening
Trosch et al. ^[36]	RT	–	1180	1400	20.4	–	PBF-LB/M (different processing parameters, e.g., layer thickness of 20 μm , different scanning strategy, vertically built specimens), no stress relief, solution treatment at 980 °C, similar two-stage aging
Trosch et al. ^[36]	650	–	860	992	14.2	–	PBF-LB/M (different processing parameters, e.g., layer thickness of 20 μm , different scanning strategy, vertically built specimens, no stress relief, solution treatment at 980 °C, similar two-stage aging

^{a)}Could not be determined because of fracture in radius.

strength increase with a decrease in the recrystallized grain fraction and an increase in the deformed grain fraction in the samples.

Ronneberg et al. also showed that the presence of pores has no effect on the yield strength of PBF-LB/316L SS.^[33] They concluded that microstructural features such as grain boundaries, chemical segregation along melt pool boundaries and cell walls, as well as heterogeneous dislocation density within the material control the yield strength. Lack-of-fusion porosity affects only ductility and failure mechanisms.

Jost et al. statistically proved for as-built PBF-LB/316L SS that porosity negatively impacted both ductility and strain at ultimate tensile strength, while elastic modulus, ultimate tensile

strength, and yield stress fairly and only moderately correlated with porosity characteristics.^[34] They found that pores above 125 μm diameter have the most significant effect on tensile performance.

As mentioned in section 2.1.1. the typical porosity of the batch of material investigated in the present study was reported in another study^[11] and was found to be <0.005%. Additional analysis of the data was made by the authors to extract the maximum pore size and shape distribution. This analysis showed that the maximum equivalent pore diameter was 57 μm and that the pore shape is predominantly round. In the light of the discussion in the previous sections, we therefore assume that porosity is not an explanation for the lower tensile strength in the PBF-LB material,

but rather see the main cause in the lower hardening capacity due to the dislocation cell structure.

It remains to be noted that the characteristic RT tensile strength values determined in our investigation on the heat-treated specimens are significantly higher than the values measured in the as-built condition by Schröder et al (see Table 5; their tests were carried out in the same lab and on the same testing machine and the PBF-LB/M specimens were processed under similar conditions).^[11] The heat treatment thus leads to an almost doubling of the 0.2% proof strength and an $\approx 40\%$ higher tensile strength. However, this is at the expense of elongation at fracture, which is reduced by almost half compared to the as-built condition.

Microstructurally, as evidenced in Figure 3a,b, the heat treatment dissolved at least partially the cellular dislocation substructure inherent to the as-built condition of the PBF-LB/M material and completely dissolved the microsegregation associated with it. It was, therefore, possible to realize the desired homogeneous precipitation of γ'' (see Figure 3c), which is also expectedly present in the REF material. Since the 0.2% proof strength of the PBF-LB material increased by $\approx 40\%$ after heat treatment and is in this condition similar to that of the REF material (see Figure 5 and Table 5), it is reasonable to argue that it is not the cellular structure but the γ'' precipitates that mainly contribute to the observed strengthening at RT of this alloy.

Piglione et al. reported tensile values for horizontally built PBF-LB/IN718 after comparable solution and precipitation annealing (but no stress relief).^[35] The reported values for the 0.2% proof strength and the tensile strength at RT are somewhat higher than our results (cf. Table 5). However, the elongation after fracture is considerably lower (7.9%), which they attributed to the relatively high material porosity. By avoiding stress relief annealing above 1000 °C, the dislocation cell structure in the work from Piglione et al. appears to be preserved while the segregation is reduced. The authors interpret the high strength as caused by the cells hindering dislocation slip, resulting in significant strain hardening. Sharma et al. characterized vertical walls of IN718 manufactured by PBF-LB/M and after different heat treatments.^[12] After a double-stage solution heat treatment followed by two-stage precipitation hardening, the tensile strength at RT in BD is lower compared to our results while the elongation at fracture is somewhat higher (cf. Table 5). They attribute the high ductility to the presence of the δ phase at grain boundaries and the dissolution of the Laves phase. Trosch et al. characterized the mechanical properties at RT and at elevated temperature for PBF-LB/IN718, applied no stress relief, but a solution treatment at 980 °C followed by a similar two-stage aging as in our study.^[36] They report characteristic strength values at RT for the vertical BD that are comparable to ours, but those at 650 °C are significantly lower than our results. However, the elongation after fracture is higher.

The manufacturing process of the specimens of the referenced work differs in several details from that of our work, as pointed out in Table 5. Not in every case, all information is available for reproducing the samples in the referenced work. This impedes clear phenomenological explanations of the differences in the presented test results, which is also not the aim of this study.

3.2.2. Low-Cycle Fatigue Tests

The LCF behavior of PBF-LB/M and REF specimens tested at RT and 650 °C is summarized in Figure 6. Figure 6a,d shows illustrative stress–strain hysteresis curves from LCF tests at half lifetime for the three strain amplitudes investigated for both material variants. The hystereses appear very similar for the same applied total strain for each variant. There is a tendency for the hystereses to be a little narrower for the PBF-LB/M material, that is, the inelastic strain is slightly lower than for the REF condition, which is consistent with the observed lower strain hardening capacity and lower ductility of PBF-LB/M in monotonic tensile tests. This trend is somewhat more pronounced for $T = 650$ °C.

The cyclic stress response curves plotted as stress range, $\Delta\sigma$, versus number of cycles, N , in Figure 6b,e show that for both material variants the fatigue behavior is characterized by cyclic softening, which is more pronounced at the higher test temperature than at RT. In addition, softening depends on the strain amplitude: for the lowest strain amplitude of 0.5%, softening is only slight, especially at RT, while at $T = 650$ °C, it is more pronounced. For the medium and high strain amplitude, significant cyclic softening is obvious for both test temperatures, especially for the higher test temperature. The cyclic stresses tend to be at RT somewhat lower for PBF-LB/M than for REF, while at 650 °C it tends to be the other way around. Softening is also less pronounced for PBF-LB/M at 650 °C than for the REF condition. This indicates that the PBF-LB/M microstructure is more stable at high temperature or that the crack initiation or propagation resistance is higher compared to the REF variant. The selected heat treatment seems to be beneficial in terms of fatigue behavior at 650 °C.

Piglione et al. investigated the LCF behavior at RT (strain amplitude $\pm 0.8\%$) of PBF-LB/IN718 after comparable solution and precipitation annealing (but no stress relief).^[35] In contrast to our observations, they observed pronounced cyclic hardening in the first cycles followed by moderate cyclic softening. Cracks initiated at large (mostly lack of fusion) pores close to the surface due to the high porosity of 0.31% in the material. Cyclic softening is often caused by dynamic recovery of dislocations. The early onset of cyclic softening after few cycles is attributed by the authors to the dislocation cells with high dislocation densities formed during solidification and is retained after their chosen heat treatment. They report that the solidification cell structure was rather stable during fatigue.

Aydinöz et al. also observed a short period of cyclic hardening followed by slight continuous cyclic softening at RT in a (single-stage) solution heat-treated and double-aged PBF-LB/IN718 alloy.^[7] They report on clearly defined cell substructures after solution annealing and the presence of γ'' -precipitates after aging in their studied material. The authors interpret the pronounced cyclic softening with the repeated shearing and the accompanying reduction in the size of the γ'' -precipitates during cyclic loading, which is well known for the wrought variant of IN718. The shearing mechanism depends on the size of the γ'' -precipitates.^[37] In an early work, Fournier and Pineau investigated the LCF behavior of conventionally heat treated forged IN718 at RT and at 550 °C.^[38] At RT, they observed an initial

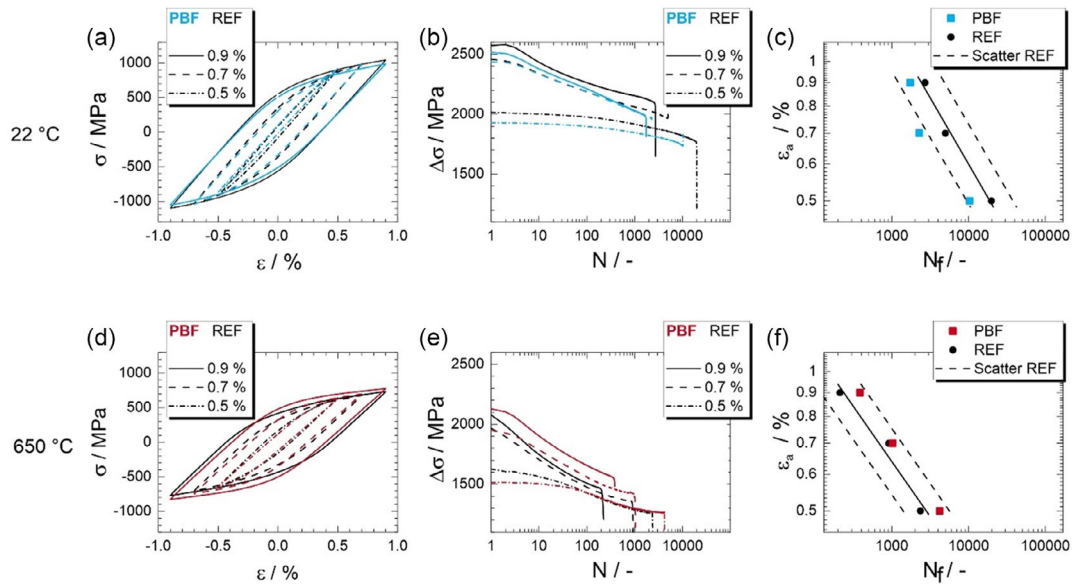


Figure 6. LCF behavior of PBF-LB/M material (blue, red) and the wrought reference material (REF, black) for different strain amplitudes at RT (upper row) and at $T = 650\text{ °C}$ (lower row): a,d) stress–strain hysteresis curves at half-life time ($N_f/2$); b,e) cyclic deformation (softening) curves; c,f) fatigue life as number of cycles to failure, N_f , with respect to expected 2x-scatter of REF material (dashed lines).

rapid strain hardening followed by softening at all strain amplitudes studied, while at 550 °C only softening occurred. TEM investigations showed that the γ'' precipitates were sheared off during the cyclic straining. They found that plastic deformation proceeded by the propagation of planar bands identified as twins. The authors further observed that twinning occurred more frequently at higher temperatures than at RT. Cracking took place generally along the interfaces between these twin bands and the matrix, but at higher temperatures and low strain rates, intergranular cracking also occurred.

Xiao et al. studied the LCF behavior of a wrought Inconel 718-based alloy at RT and 650 °C which was heat treated using a commercial approach.^[39] They report that fatigue loading at both test temperatures resulted in the formation of planar deformation bands and shearing of γ'' - and γ' -precipitates by paired dislocations. They further noticed planar slip and the formation of slip bands as the paired dislocations could not cross-slip. The spacing and the width of the bands were found to be almost independent of the amplitude of the cyclic plastic strain.

It is certainly reasonable to assume that cyclic deformation in the PBF-LB/M material will lead to similar interactions between dislocations and precipitates as already studied in detail for the wrought variants of IN718. Nevertheless, the question of the role of cell structures in the AM material in the fatigue deformation process remains open. Possibly, they could determine the tendency of somewhat slower softening in the PBF-LB/M variant observed in our tests. We will investigate this question further in the future with detailed work on microstructure evolution, as this was not possible within the scope of this study.

Finally, the fatigue lives are summarized in Figure 6c,f. Overall, the lifetimes of both material variants decrease with increasing temperature. At RT, the lifetimes of the PBF-LB/M variant are all slightly lower than those of the REF condition.

This could be due to the lower ductility and higher grain size (the damage behavior will be discussed in more detail in section 3.4). However, in terms of the scatter expected for the REF condition, for which a factor of 2 is usually assumed (indicated by dashed lines in Figure 6c,f), the lifetimes of PBF-LB/M are still within or, for 0.7%, just outside the scatter band. It must be noted that the statistical basis for the evaluation of the fatigue results is small since only a limited number of tests and no repeat tests were performed, as the aim of our study was to make an initial assessment of the fatigue behavior (statistical validation was not the objective). At $T = 650\text{ °C}$, the ratio of the lifetimes behavior is inverted: fatigue lives of the PBF-LB/M variant are all slightly higher than those of the REF condition but fall into the scatter band (factor 2) throughout. The slower softening of the PBF-LB/M material might contribute to the slightly increased fatigue life.

In contrast to our results, Mostafaei et al. reported in their review that the AM variant of IN718 shows slightly higher fatigue life at RT than at high temperature.^[9] However, results from load-controlled HCF tests were summarized in their publication, while our LCF tests were strain controlled, which may explain the difference.

There are only a limited number of publications so far that have investigated the LCF behavior of additively manufactured IN718, and especially for studies at high temperature, there are still large gaps in published data. The lifetimes of (single stage) solution heat-treated and double-aged PBF-LB/IN718 alloy at RT observed by Aydınöz et al. are clearly lower than in our study.^[7] This could be related to the higher porosity in their material, which they report as 0.1%. They found that cracks initiated at pores which are present in the specimen volume.

Nezhadfar et al. studied the LCF behavior of a laser-based direct energy deposition (DED-LB/M)-processed IN718 alloy

(with single-solution heat treatment followed by double aging) at RT and at 650 °C in strain-controlled fatigue tests up to 10^6 cycles.^[40] At high strain amplitudes ($\geq 0.6\%$) in the LCF regime, the fatigue life of the DED-LB/M material was slightly higher at RT than at high temperature, which is similar to our results, although the difference is greater in our study. They report that cracks initiated from hard particles and/or pores close to the surface and propagated transgranular. On the other hand, they observed that with decreasing strain amplitudes (and decreasing cyclic plasticity, i.e., in the HCF regime, $>10^4$ cycles) the fatigue lives are comparable. They attribute the inferior LCF behavior of the DED-LB/M material at elevated temperature to the formation of more δ and Laves phases during fatigue testing at high temperature because these brittle phases may fracture at high strains, create secondary cracks, and accelerate fatigue damage. The authors also report that the fatigue resistance of the DED-LB/M variant at elevated temperature was similar to the wrought counterpart.

Mostafaei et al. pointed out that the mechanisms of cyclic behavior and fatigue failure in AM alloys are particularly complex.^[9] The origin is found in a number of different, possibly interacting influencing variables such as microstructural features and different types of process-induced defects. The discussion shows that further and more detailed investigations are necessary for safe use of AM IN718 in the future. This concerns both the determination of fatigue data at different temperatures and the deformation and damage mechanisms.

3.3. Fracture under Monotonic Loading

Figure 7 shows distinct differences in fracture behavior in tensile testing. The REF material shows clear necking of the specimens near the fracture surface at both test temperatures (Figure 7a,e). In contrast, the PBF-LB/M material does not exhibit necking. (Figure 7b,f). At RT, the fracture is characterized by pronounced shear lips in the REF material (Figure 7a,c), which is not the case in the PBF-LB/M material (Figure 7b,d). The checkerboard pattern is visible on the fracture surface of the PBF-LB/M material (Figure 7d,h), indicating a highly different deformation behavior of the microstructure.

3.4. Fracture under LCF Loading

The fracture surfaces of the REF and PBF-LB/M material also appear very different after fatigue failure at RT, as Figure 8 illustrates. The location of the crack initiation is somewhat more difficult to detect in the PBF-LB/M than in the REF material. The semilenticular regions of the fatigue crack tend to be smaller in the PBF-LB/M material. This is particularly evident when comparing Figure 8d,j, or Figure 8f,l. This suggests that specimen failure or residual fracture in PBF-LB/M is initiated at significantly smaller macrocrack lengths, indicating that local stress concentrations at the crack tip can only be relieved to a limited extent by plastic deformation in the PBF-LB/M material.

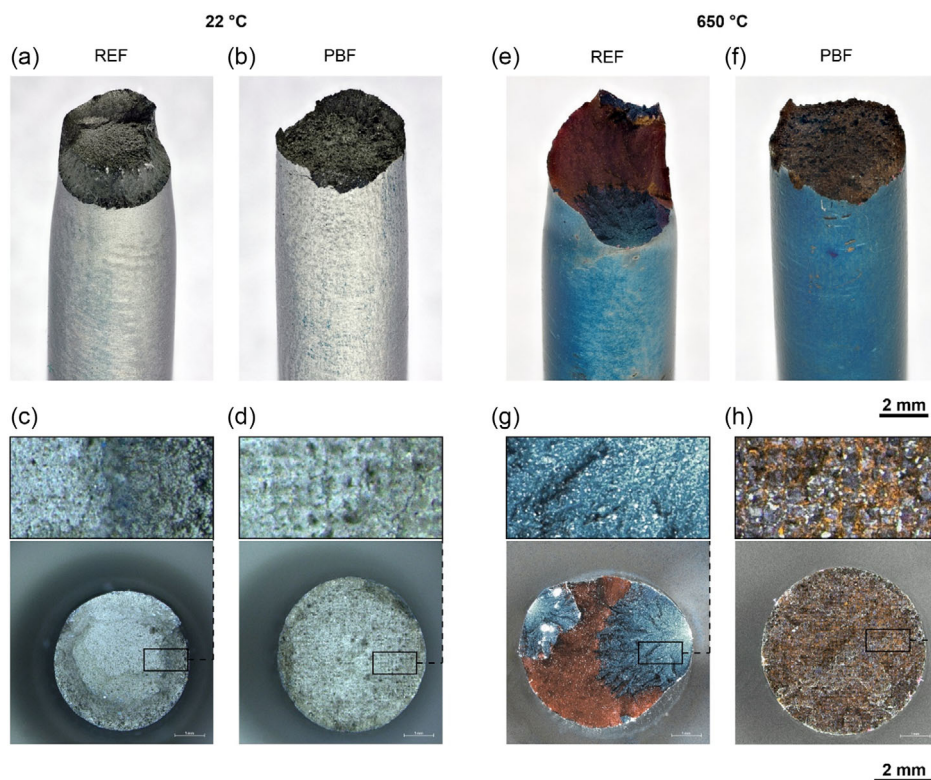


Figure 7. Fractured tensile specimens perspective view (macro photo in a,b) and e,f)) and fractured surfaces in the respective top view (OM). The small rectangular images on top represent enlarged details. a–d) RT and e–h) after testing at 650 °C.

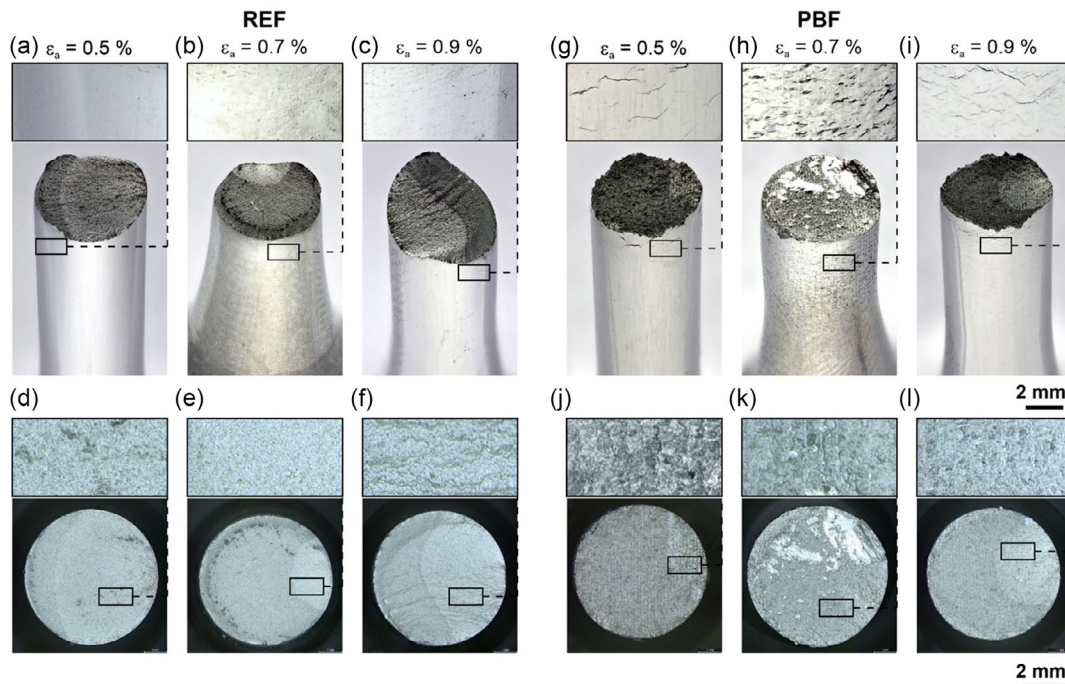


Figure 8. Fracture surfaces of the LCF specimens tested at RT (left REF, right PBF-LB/M). The top row shows photographs of the fractured specimens, the bottom row OM images (top view) of the fracture surfaces (note: in the bottom row, the supposed crack initiation is always on the right and might be rotated to the top row). The small rectangular images on top represent enlarged details.

It is also anticipated that the locally systematically heterogeneous microstructure described in section 3.1.1 will deform very differently, especially in regions where very fine and coarse grains meet (cf. Figure 2c,d), causing micromechanical gradients. These, in combination with local stress concentrations at the front of propagating cracks, will possibly govern crack growth and branching. The checkerboard pattern on the PBF-LB/M fracture surfaces is also clearly visible, Figure 8j–l. (Note: the white areas in Figure 8h,k are probably due to contact in the compression cycle toward the end of the test, which significantly altered the topography). It is also noticeable that, in contrast to the REF specimens, the lateral surfaces of the PBF-LB/M specimens show many microcracks characterized by frequent, systematic changes in direction that are, thus, likely linked to the PBF-LB/M-typical microstructure. The microcracks even appear with high-density several millimeters away from the fracture surface (compare Figure 8g–i).

The characteristics of the fractured test pieces and the fracture surfaces of the specimens subjected to fatigue at 650 °C, which are shown in Figure 9, are similar to those at RT (cf. Figure 8). Due to the tinting colors caused by oxidation, the characteristics of the cracks are even more obvious. In each case, the areas of stable crack growth appear blue on the fracture surface, while those of residual fracture are gray or beige. It can also be clearly seen here that several crack initiation sites exist in the PBF-LB/M variant (Figure 9j–l), which is not the case in the REF variant. In addition, large steps are visible in the BD direction, indicating that cracks do not grow only in one plane (Figure 9g–i).

3.5. PBF-LB/M Fatigue Crack Propagation

Figure 10 shows BSE–SEM images of the fracture surfaces of the failed PBF-LB/M LCF specimens in the region of stable fatigue crack propagation, that is, in the light gray and bluish regions in Figure 8 and 9, respectively. Note that the loading direction was parallel to BD. The checkerboard pattern can be readily seen, as in the OM images. Even though the backscatter image shows little topography, it can be partially recognized that the crack front does not run smoothly through the material, but changes its plane here and there, creating steps. Moreover, in the tests at RT with high strain amplitudes ($\geq 0.7\%$) and especially in all high-temperature tests, secondary cracks (examples marked by black arrows) systematically appear at the PEGM–SGwRP transitions (corresponding to the transitions between blue and green areas in Figure 2c). This indicates that the crack paths are a result of sharp micromechanical gradients at these transitions. In addition, grains in $\langle 001 \rangle$ orientations (red in Figure 2a) are found in the PEGM regions in large numbers, which (at least at RT) represent the preferred crack growth directions in polycrystalline Inconel with a significant proportion of $\langle 001 \rangle \parallel \text{BD}$ grain orientations.^[41] In the high-temperature tests, the number of secondary cracks is even greater. It is possible that the high temperature additionally leads to creep damage of the grain boundaries (i.e., grain boundary sliding), which favors intergranular crack growth.

BSE–SEM images of microcracks in polished longitudinal sections are shown in Figure 11, illustrating the growth of short secondary cracks across multiple grains in the characteristic

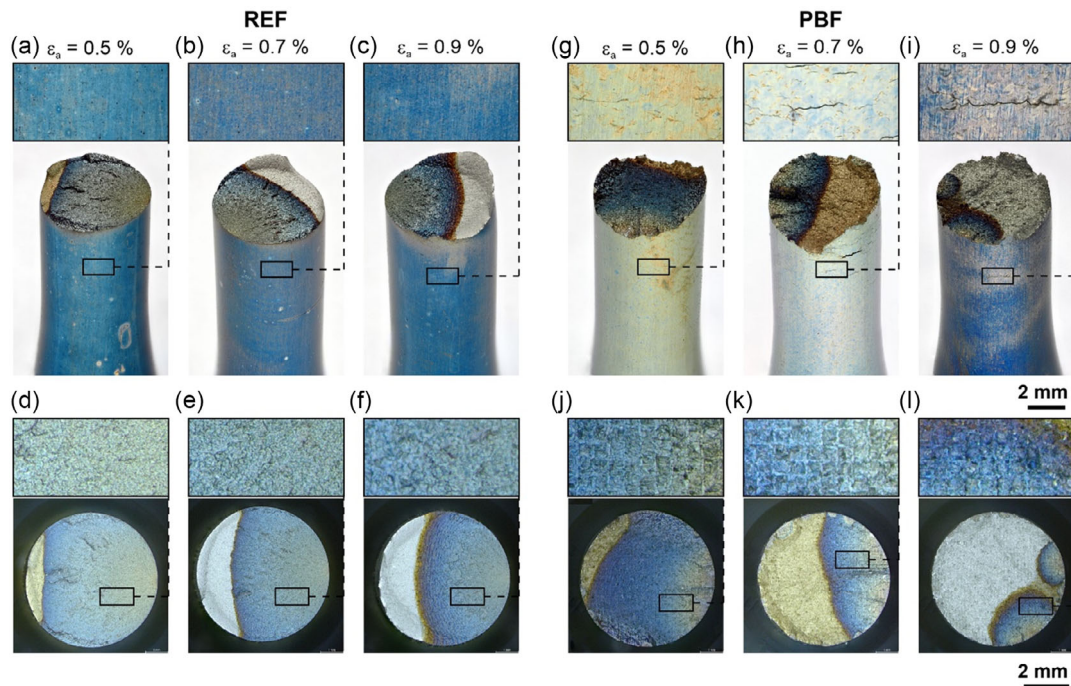


Figure 9. Fracture surfaces of the LCF specimens tested at 650 °C (left REF, right PBF-LB/M). The top row shows photographs of the fractured specimens, the bottom row OM images (top view) of the fracture surfaces (note: in the bottom row, the supposed crack initiation is always on the right and might be rotated to the top row). The small rectangular images on top represent enlarged details.

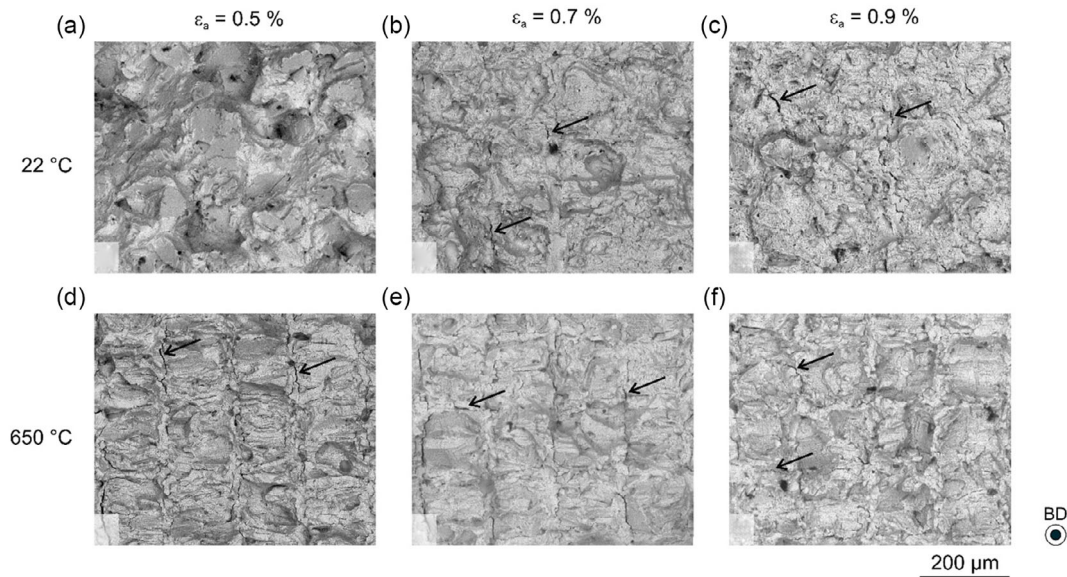


Figure 10. Fracture surfaces of PBF-LB/M fatigue specimens in the region of stable fatigue crack propagation at different strain amplitudes and test temperatures (BSE–SEM). Secondary cracks are marked by black arrows. Fatigue loading direction was parallel to BD.

PBF-LB/M microstructure, starting from the outer surface on the left side. (Note that similar to sections of the undeformed PBF-LB/M material (cf. Figure 2), the microstructure observed depends on where exactly the PBF-LB/M microstructure is cut during preparation due to the recurring periodic features.

Hence, it is not always possible to find the optimal cutting plane, especially in deformed specimens with rotational symmetry. This must be considered when interpreting the results.) Such microcracks were found particularly on PBF-LB/M specimens after fracture, sometimes in high density on the lateral surfaces

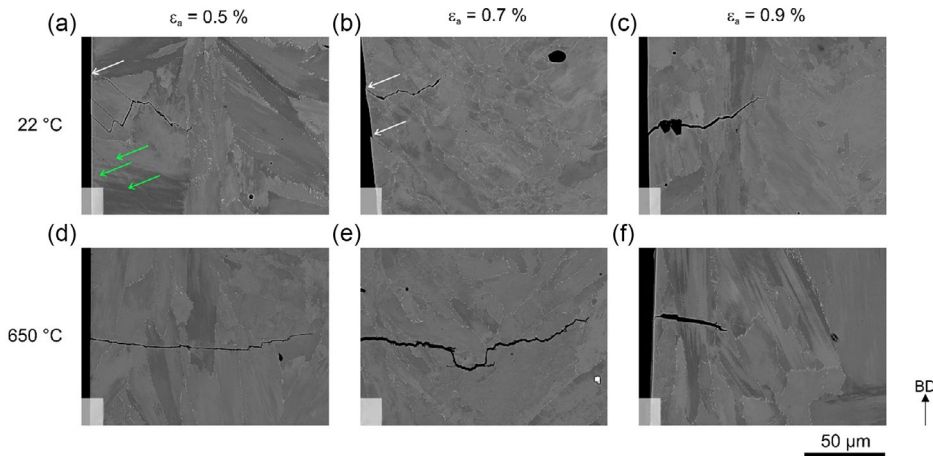


Figure 11. Microcracks in polished longitudinal sections of PBF-LB/M fatigue specimens at different strain amplitudes and test temperatures (BSE-SEM). White arrows mark steps on surface, green arrows indicate slip bands. Fatigue loading direction was parallel to BD.

(Figure 8g–i and 9g–i). Clearly, the cracks always initiate on the surface and not in the volume. In the case of fatigue at RT (Figure 11a–c), the cracks initially tend to grow transgranular at about 45° to the applied axial load. Larger grain regions shear off and cause steps on the specimen surfaces (examples marked by white arrows). There appears to be a correlation between the slip bands formed (examples marked by green arrows in Figure 11a) and crack initiation and growth of short cracks. All cracks are very short, since they are secondary cracks that have not progressed very far, unlike the macrocrack that initiated the final failure. Their growth, therefore, as is well known for short crack growth, depends strongly on the local microstructural conditions, and cracks often change their directions when they reach adjacent grains.^[42] A tendency toward deflection and branching is also evident.

Figure 11d–f shows the crack paths after fatigue at 650 °C. In contrast to the results at RT, the secondary cracks tend to propagate perpendicular to the loading direction initially and are, thus, more transgranular. At the specimen surface, in contrast to RT, the shear steps are virtually absent, indicating that at 650 °C the fatigue slip bands apparently play only a minor role here. It should be noted that the cracks shown in Figure 11d,f coincidentally propagate through the PEGM region, which features mostly elongated grains or grain regions of similar <001> orientation (cf. side faces of the IPF cube in Figure 2a). The grains are cut through relatively straight and apparently take a crystallographic easy path. In Figure 11e, the depicted crack grows through a column of stacked grains (cf. SGwRP region, Figure 2b) and tends to grow intergranularly and sometimes changes direction (center of image), for example, due to preferential grain orientations at triple points, critical MOs between neighboring grains or characteristic precipitation features.

The crack deflections and branching have different causes depending on the length scales. At a larger length scale, crack propagation occurs preferentially in <001> direction, so that the checkerboard pattern develops in the fracture surfaces and secondary cracks run along the checkerboard edges (PEGM grains). Prost et al. showed that the growth rate of fatigue cracks

in PBF-LB/IN718 seems to be mainly determined by the crystallographic texture.^[43] They observed a higher fatigue crack growth rate in a variant with <001> orientation than in a more isotropic material (test condition: loading parallel to BD, *z*, notch orientation orthogonal to *z*; *T* = 550 °C). They observed transgranular crack growth under those test conditions and point out that the crack growth mechanism strongly depends on the microstructure.

The orientation dependence of the crack propagation possibly continues to the subgrain level, so that microscopic directional changes from subgrain to subgrain also occur within appropriately oriented grains. δ phase precipitates at grain boundaries (as implied by the frayed appearance of crack flanks in, e.g., Figure 11d,e), stress fields between (more often fine-grained) PEGM and (coarse-grained) SGwRP regions, and micromechanical gradients contribute to crack propagation at the micrometer scale. It should be noted, however, that the studies were limited to 2D images, but cracks also bend or branch perpendicular to the image plane without being visible here. Thus, the crack path is influenced by the specimens' and test pieces' manufacturing strategy and by the morphological anisotropy of the microstructure and the relative loading direction. If, for example, the specimens had been printed horizontally and the structure of PEGM and their long-grain boundaries were oriented perpendicular to the loading direction, it can be reasonably assumed that crack propagation would then have occurred in these horizontal PEGM regions along those grain boundaries and not transgranular through the favorably oriented grain. This hypothesis would have to be proven with further investigations, which was not possible within the scope of this study.

4. Conclusion

The Ni-based alloy Inconel 718, produced by PBF-LB/M applying a bidirectional scan strategy with 90° rotation after each layer and subjected to a four-step heat treatment (homogenization, solution annealing, double aging), was characterized regarding its hierarchical microstructure in the heat-treated condition. Its

tensile and LCF behavior at RT and 650 °C was determined. The following conclusions are drawn: 1) Major unique microstructural features produced in the PBF-LB/M process, such as grain size and morphology, and a periodically graded structure of stacked grains forming columns separated by regions with predominantly elongated grain morphology in BD, are mostly retained after the applied four-step heat treatment. Furthermore, the microsegregation and dislocation density related to the cellular structure are reduced, facilitating a homogeneous γ'/γ'' precipitation; 2) Compared to the as-built state reported in a previous study, the heat treatment enhances the proof strength by a factor of about 2 at the cost of the elongation at fracture (reduced by almost half), ductility, and strain hardening capacity. The heat-treated PBF-LB/M variant achieves monotonic tensile and LCF properties comparable to the wrought variant: Elastic and yield properties are comparable at both temperatures while UTS, ductility, and strain hardening capacity are slightly lower for the PBF-LB/M variant; 3) Accordingly, slightly lower inelastic strains emerge under low- and high-temperature LCF conditions for the PBF-LB/M compared to the wrought variant. The fatigue life of the PBF-LB/M variant at RT is slightly lower than that of the wrought material, while at 650 °C, it is vice versa. The cyclic stress response for both material variants is characterized by cyclic softening; 4) The crack propagation appears to be mainly influenced by the grain orientation and morphology and the presence of δ phase at the grain boundaries. Multiple crack initiation sites emerge at the PBF-LB/M specimen surfaces under LCF loading at room and high temperature, which are not associated with PBF-LB/M volume defects. Especially in the microstructurally heterogeneous material regions, significant crack branching and deflection are observed. This indicates that the cracks are a result of both sharp micromechanical gradients and local clusters of crystallites with $\langle 001 \rangle$ orientation which are favored for crack propagation; and 5) The propensity of the PBF-LB/M material for systematic crack branching and deflection causes uneven crack fronts with mixed-mode propagation characteristics. Hence, due to the associated energy dissipation by crack deflection and branching, fatigue lives approaching those of the wrought material are achieved at RT despite the comparatively large average grain size and the tendency to pronounced slip band formation.

Consequently, the heat treatment strategy appears to be very promising for the given PBF-LB/M microstructure in meeting the advanced mechanical requirements of IN718 when subjected to high-temperature LCF.

Acknowledgements

This work was supported by the BAM Focus Area Materials Project AGIL "Microstructure development in additively manufactured metallic components: from powder to mechanical failure". The authors would like to express their gratitude to the following colleagues at BAM for their numerous support, which contributed to the achievement of this work: Mr. S. Thärig for the metallographic preparation, optical microscopy, and digital photography, Ms. A. Zunkel for optical emission spectrometry measurements, Mr. R. Saliwan-Neumann for scanning electron microscopy, electron backscatter, and EDS, Mr. R. Hesse for the focused ion beam target preparation, Ms. M. Buchheim and Ms. E. Sonnenburg for fractographic investigations, Mr. J. Schröder for the additional analysis of

the X-ray computed tomography data, and Mr. J. Schröder and Dr. G. Nolze for valuable discussions.

Open Access funding enabled and organized by Projekt DEAL.

Conflict of Interest

The authors declare no conflict of interest.

Data Availability Statement

The data that support the findings of this study are available from the corresponding author upon reasonable request.

Keywords

additive manufacturing, fatigue damages, heat treatments, Inconel 718, laser powder bed fusion, low-cycle fatigue, tensile strengths

Received: December 11, 2023

Revised: January 27, 2024

Published online:

- [1] J. O. Milewski, in *Additive Manufacturing of Metals*, Springer, Cham **2017**.
- [2] T. H. Becker, P. Kumar, U. Ramamurty, *Acta Mater.* **2021**, 219, 117240.
- [3] T. DebRoy, H. L. Wei, J. S. Zuback, T. Mukherjee, J. W. Elmer, J. O. Milewski, A. M. Beese, A. Wilson-Heid, A. De, W. Zhang, *Prog. Mater. Sci.* **2018**, 92, 112.
- [4] B. Merz, K. Poka, R. Nilsson, G. Mohr, K. Hilgenberg, in *Lasers in Manufacturing (LiM) 2023*, WLT, 1.
- [5] G. Liu, X. Zhang, X. Chen, Y. He, L. Cheng, M. Huo, J. Yin, F. Hao, S. Chen, P. Wang, S. Yi, L. Wan, Z. Mao, Z. Chen, X. Wang, Z. Cao, J. Lu, *Mater. Sci. Eng. R* **2021**, 145, 100596.
- [6] M. Laleh, E. Sadeghi, R. I. Revilla, Q. Chao, N. Haghdadi, A. E. Hughes, W. Xu, I. De Graeve, M. Qian, I. Gibson, M. Y. Tan, *Prog. Mater. Sci.* **2023**, 133, 101051.
- [7] M. E. Aydinöz, F. Brenne, M. Schaper, C. Schaak, W. Tillmann, J. Nellesen, T. Niendorf, *Mater. Sci. Eng. A* **2016**, 669, 246.
- [8] S. Gribbin, S. Ghorbanpour, N. C. Ferreri, J. Bicknell, I. Tsukrov, M. Knezevic, *Mater. Charact.* **2019**, 149, 184.
- [9] A. Mostafaei, R. Ghiaasiaan, I. T. Ho, S. Strayer, K.-C. Chang, N. Shamsaei, S. Shao, S. Paul, A.-C. Yeh, S. Tin, A. C. To, *Prog. Mater. Sci.* **2023**, 136, 101108.
- [10] J. Schneider, L. Farris, G. Nolze, S. Reinsch, G. Cios, T. Tokarski, S. Thompson, *J. Manuf. Mater. Process.* **2022**, 6, 20.
- [11] J. Schröder, A. Evans, E. Polatidis, J. Čapek, G. Mohr, I. Serrano-Munoz, G. Bruno, *J. Mater. Sci.* **2022**, 57, 15036.
- [12] S. Sharma, K. Palaniappan, V. D. Mishra, S. Vedantam, H. Murthy, B. C. Rao, *Metall. Mater. Trans. A* **2023**, 54, 270.
- [13] S. Mukhopadhyay, H. Sriram, C. H. Zenk, R. DiDomizio, A. J. Detor, R. W. Hayes, G. B. Viswanathan, Y. Wang, M. J. Mills, *Metals* **2021**, 11, 1897.
- [14] A.-C. Yeh, K.-W. Lu, C.-M. Kuo, H.-Y. Bor, C.-N. Wei, *Mater. Sci. Eng. A* **2011**, 530, 525.
- [15] Y. Desvallées, M. Bouzidi, F. Bois, N. Beaudé, in *Superalloys 718, 625, 706 and Various Derivatives* (Ed: B. A. Loria), The Minerals, Metals & Materials Society, Warrendale, PA, USA **1994**, pp. 281.
- [16] S. Li, J. Zhuang, J. Yang, Q. Deng, J. Du, in *Superalloys 718, 625, 706 and Various Derivatives* (Ed: B. A. Loria), The Minerals, Metals & Materials Society, Warrendale, PA, USA **1994**, pp. 545.

- [17] B. Rehmer, F. Bayram, L. A. Ávila Calderón, G. Mohr, B. Skrotzki. BAM reference data: Temperature-dependent Young's and shear modulus data for additively and conventionally manufactured variants of Ni-based alloy Inconel IN718. Zenodo, **2023**.
- [18] ASTM F 3301a, in *Standard for Additive Manufacturing – Post Processing Methods – Standard Specification for Thermal Post-Processing Metal Parts Made Via Powder Bed Fusion*, ASTM International, West Conshohocken **2018**.
- [19] SAE AMS 5663P, *Nickel Alloy, Corrosion- and Heat-Resistant, Bars, Forgings, Rings, and Stock for Forgings and Rings, 52.5Ni – 19Cr – 3.0Mo – 5.1Cb (Nb) – 0.90Ti – 0.50Al – 18Fe, Consumable Electrode or Vacuum Induction Melted, 1775 °F (968 °C) Solution and Precipitation Heat Treated*, SAE International, Warrendale, PA, USA **2022**.
- [20] ASTM B 637, in *Standard Specification for Precipitation-Hardening and Cold Worked Nickel Alloy Bars, Forgings, and Forging Stock for Moderate or High Temperature Service*, ASTM International, West Conshohocken **2018**.
- [21] ISO 6892-1, in *Metallische Werkstoffe – Zugversuch – Teil 1: Prüfverfahren bei Raumtemperatur*, International Organization for Standardization, Geneva **2019**.
- [22] ISO 6892-2, in *Metallische Werkstoffe – Zugversuch – Teil 2: Prüfverfahren bei Erhöhter Temperatur*, International Organization for Standardization, Geneva **2018**.
- [23] ISO 12106, in *Metallische Werkstoffe – Ermüdungsprüfung – Einachsige Prüfung mit der Dehnungskontrollierten Methode*, International Organization for Standardization, Geneva **2017**.
- [24] DIN EN ISO 9513, in *Metallische Werkstoffe – Kalibrierung von Längenänderungs-Messeinrichtungen für die Prüfung mit Einachsiger Beanspruchung (ISO 9513:2012 + Cor. 1:2013); Deutsche Fassung EN ISO 9513:2012*, Beuth Verlag GmbH, Berlin **2013**.
- [25] A. Charmi, R. Falkenberg, L. Ávila, G. Mohr, K. Sommer, A. Ulbricht, M. Sprengel, R. Saliwan Neumann, B. Skrotzki, A. Evans, *Mater. Sci. Eng. A* **2021**, 799, 140154.
- [26] L. A. Ávila Calderón, B. Rehmer, S. Schriever, A. Ulbricht, L. Agudo Jácome, K. Sommer, G. Mohr, B. Skrotzki, A. Evans, *Mater. Sci. Eng. A* **2022**, 830, 142223.
- [27] DIN ISO 13067, in *Microbeam Analysis – Electron Backscatter Diffraction – Measurement of Average Grain Size*, Beuth Verlag GmbH, Berlin **2021**.
- [28] A. Ulbricht, L. A. Ávila Calderón, K. Sommer, G. Mohr, A. Evans, B. Skrotzki, G. Bruno, *Adv. Eng. Mater.* **2023**, 25, 2201581.
- [29] P. V. Cobbinah, S. Matsunaga, Y. Yamabe-Mitarai, *Adv. Eng. Mater.* **2023**, 25, 2300819.
- [30] B. Rehmer, F. Bayram, L. A. Ávila Calderón, G. Mohr, B. Skrotzki, *Sci. Data* **2023**, 10, 474.
- [31] G. Nolze, M. Jürgens, J. Olbricht, A. Winkelmann, *Acta Mater.* **2018**, 159, 408.
- [32] H. E. Sabzi, E. Hernandez-Nava, X.-H. Li, H. Fu, D. San-Martín, P. E. J. Rivera-Díaz-del-Castillo, *Mater. Des.* **2021**, 212, 110246.
- [33] T. Ronneberg, C. M. Davies, P. A. Hooper, *Mater. Des.* **2020**, 189, 108481.
- [34] E. W. Jost, J. C. Miers, A. Robbins, D. G. Moore, C. Saldana, *Addit. Manuf.* **2021**, 39, 101875.
- [35] A. Piglione, B. Attard, V. Vieira Rielli, C.-T. Santos Maldonado, M. M. Attallah, S. Primig, M.-S. Pham, *Addit. Manuf.* **2021**, 47, 102347.
- [36] T. Trosch, J. Strößner, R. Völkl, U. Glatzel, *Mater. Lett.* **2016**, 164, 428.
- [37] M. Sundararaman, P. Mukhopadhyay, S. Banerjee, *Acta Metall.* **1988**, 36, 847.
- [38] D. Fournier, A. Pineau, *Metall. Trans. A* **1977**, 8, 1095.
- [39] L. Xiao, D. L. Chen, M. C. Chaturvedi, *Scr. Mater.* **2005**, 52, 603.
- [40] P. D. Nezhadfar, A. S. Johnson, N. Shamsaei, *Int. J. Fatigue* **2020**, 136, 105598.
- [41] G. Liu, S. Winwood, K. Rhodes, S. Biroasca, *Int. J. Plast.* **2020**, 125, 150.
- [42] S. Suresh, in *Fatigue of Materials*, Cambridge University Press, Cambridge **2004**.
- [43] M. Prost, A. Köster, D. Missoum-Benziane, S. Dépinoy, L. Ferhat, M. Rambaudon, V. Maurel, *Addit. Manuf.* **2023**, 61, 103301.